RSC Advances

ROYAL SOCIETY OF CHEMISTRY

www.rsc.org/advances

Graphical Abstract:

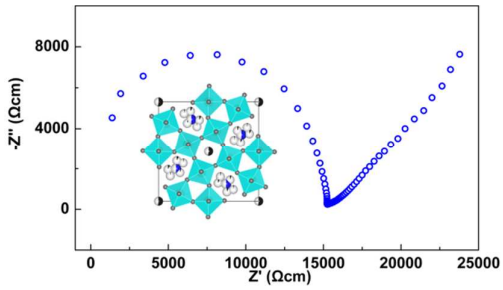

70×39.6 mm (700 × 700 dpi)

Textual Abstract:

Tetragonal tungsten bronze compound, $BaBiNb_5O_{15}$, is found to be a new type oxide ion conductor, showing a total electrical conductivity of 3×10^{-4} S/cm at 600 °C.

RSC Advances

PAPER

Structure and Oxide-ion Conductivity in Tetragonal Tungsten Bronze $BaBiNb_5O_{15}$

Received 00th January 20xx,
Accepted 00th January 20xx

DOI: 10.1039/x0xx00000x

www.rsc.org/

HongqiangMa[a], Kun Lin[a], LonglongFan[a], YangchunRong[a], Jun Chen[a] , JinxiaDeng[a,b], LaijunLiu[c], Shogo Kawaguchi[d],Kenichi Kato[e], Xianran Xing*[,a]

The crystal structure and electrical properties of a tetragonal tungsten bronze (TTB) compound, $BaBiNb_5O_{15}$ were investigated by high-resolution synchrotron X-ray powder diffraction and AC impedance spectroscopy. The compound is a new type oxide ion conductor, showing a total electrical conductivity of 3×10^{-4} S/cm at 600 °C and relatively small activation energy (0.3-0.5eV). It is suggested that the large amount of cationic vacancies in A sites, the large free space created by the large Ba^{2+}cations, and the splits of Bi atoms are in favor of oxygen ions migration. This stable tungsten bronze compound $BaBiNb_5O_{15}$ with a moderate oxide-ion conductivity showspotential applications in SOFC anode, amperometric gas sensors, and active catalyst supports.

1. Introduction

Tetragonal tungsten bronze (TTB) type materials are a big family of functional compounds that are composed of layered corner sharing octahedra framework. The general formula of TTB-type structure can be formulated as $(A2)_4(A1)_2(C)_4(B1)_2(B2)_8O_{30}$, where A1, A2, and A3 are quadrangle (12-coordinated), pentagonal (15-coordinated), and triangular (9-coordinated) tunnels respectively.[1] B1 and B2 are the octahedral sites. Generally, A1 and A2 sites can be fully or partially occupied by larger cations, like alkaline, alkaline earth , rare earth, bismuth or lead[2]; while small A3 sites can be filled with very small ions such as Li^+ ions but are typically vacant (see Fig. S1. in ESI†).[3]The structures and dielectric properties have been widely investigated due to their instinct crystalline sites and compositional flexibility.[4-10]

Oxide materials that exhibit oxygen ion conductivity have stirred a great deal of interests due to their wide applications such as oxygen separation membranes, gas sensors, catalysts, electrode and electrolyte for solid-oxide fuel cells (SOFCs).[11-14]One such family of oxides that were widely studied focus on the perovskite structure. For example, (Sr,Mg)-doped $LaGaO_3$ shows higher ionic conductivity than the conventional zirconia-based electrolyte like YSZ at moderate temperatures,[15] whereas the mixed ionic-electronic conductors like doped $La_{1-x}Sr_xMnO_3$ and $La_{1-x}Sr_xCoO_3$ are widely used as cathode material in SOFCs.[16] Computer simulations have shown that oxygen ion migration occurs by a hopping mechanism between adjacent oxygen sites along a BO_6 octahedron edge, with a slightly curved trajectory accompanied by outward relaxation of adjacent cations,[17,18] and the migrating ion moves through the center of a triangle (or saddle-point) defined by two A site cations and one B site cation.[19,20] As is known to us, TTB structured compounds possess similar network of corner-sharing BO_6octahedra (with similar saddle-points in lattice). Moreover, the larger pentagonal tunnels and the vacancies (cationic vacancies) in A1 and A2 sites may provide more free space for oxygen ions migration and minimize the migration energy. However, few reports were addressed on the oxide-ion conductivity concerning TTB oxides. A. Kaiser et al. investigated $(Ba/Sr)_3Nb_4TiO_{15}$ as anode materials for SOFCs, which revealed respectable conductivities (~10 S/cm at 930°C) under reducing conditions, but suffered from poor oxygen ion conductivity.[21] Similarly, M. Prades et al.[22] investigated electrical properties of oxygen-deficient TTB ceramics $Ba_2NdTi_{2+x}Nb_{3-x}O_{15-x/2}$, in which only small amount of oxygen vacancy and low oxide ion conduction can be obtained by varying the Ti/Nb ratio. More recently, X. Kuang et al. studied nonstoichiometric TTB-type compounds $Ba_{0.5-x}TaO_{3-x}$, nevertheless,

[a]Department of Physical Chemistry,[b] Department of Chemistry, University of Science and Technology Beijing, Beijing 100083, China.*e-mail: xing@ustb.edu.cn
Tel: + 86-10-62334200 Fax: + 86-10-62332525
[c]State Key Laboratory Breeding Base of Nonferrous Metals and Specific Materials Processing, Guilin University Of Technology, Giulin 541004, China
[d]Japan Synchrotron Radiation Research Institute (JASRI)1-1-1, Kouto, Sayo-cho, Sayo-gun, Hyogo 679-5198, Japan
[e] RIKEN SPring-8 Center, Sayo, Hyogo 679-5148, Japan
Electronic Supplementary Information (ESI) available: Structure model of TTB, SEM micrograph of BBN, Complex impedance plots of BBN measured in different atmospheres, XRD patterns of BBN at different temperatures, XRD patterns of BBN, SBN, and BBNT samples, cell parameters of BBN and SBN versus temperature, Rietveld pattern of BBNT, selected bond lengths of BBN. complex impedance plots at 250°C and 400 °C and for YSZ-coated samples. See DOI: 10.1039/x0xx00000x

the highly nonstoichiometric $(TaO)^{3+}$-containing phase exhibits migration of Ba^{2+}cations rather than that of oxygen ions.[23]

In this work, we report a Bi-based TTB-type oxide, $BaBiNb_5O_{15}$ (BBN). It is a stable oxygen ion conductor with electrical conductivity of ~3×10^{-4} S/cm at 600 °C, which is much larger than any other the reported TTB compounds and may have potential applications in SOFC anode, amperometric gas sensors and active catalyst supports.[12] The structure of BBN was characterized by means of high-resolution synchrotron X-ray powder diffraction (SPD). The electrical properties were measured by AC impedance spectroscopy. Two other compounds, $Ba_2BiNb_3Ti_2O_{15}$ (BBNT) and $SrBiNb_5O_{15}$ (SBN), are also synthesized for comparison. This study shows TTB-type compounds may be a new family of oxygen ion conducting materials.

2. Experimental

BBN ceramics were synthesized by a solid state method using $BaCO_3$ (99%), Nb_2O_5 (99.99%), and Bi_2O_3 (99.9%) as starting materials. The ball-milled powders according to aimed stoichiometry were sintered at 800 °C for 4 h. The calcined products were ball milled again for 4 h and then pressed into pellets uniaxially. The pellets were fired at 1240 °C for 2 h, covered with some calcined powder to reduce Ba and Bi-loss during firing process. Pellet density was estimated using the Archimedes method. The raw materials $BaCO_3$, Nb_2O_5, Bi_2O_3, TiO_2 (99.5%), and $SrCO_3$ (99.5%) were used for preparation of BBNT and SBN using the same method as mentioned above. High-angular resolution synchrotron X-ray powder diffraction (SPD) data were collected using a Debye–Scherrer camera with an imaging plate on beam line BL02B2 at SPring-8, Japan (RT; wavelength = 0.9980 Å). The structure was refined by Rietveld method using Jana2006 software.

AC impedance spectroscopy measurements from 200 °C to 600 °C in air were carried out with a Solartron SI 1260 impedance analyzer over the frequency range 0.1Hz to 1MHz, with an AC measuring voltage of 100 mV. Dielectric parameters were measured as a function of temperature at fixed frequency using an impedance analyzer (Agilent 4294A). Before measurements, silver paste was coated onto both sides of the polished pellet as an electrode and fired at 650 °C for 30 min to burn out the organic components. The complex impedance data were corrected for sample geometry (thickness/area of pellet) and analysed using Zview software (version 3.4b Scribner Associates Inc.,USA). The AC impedance spectra were also measured on the BBNT and SBN pellets for comparison. Impedance measurements of BBN were also performed under Air and Ar gas flows to examine whether the impedance data changes with oxygen partial pressure, which provided some information about possible oxide ion conduction in BBN ceramics.

3. Results and discussion

3.1 Crystal Structure

The high-angular resolution of the SPD profile makes it possible to determine the crystal structure of BBN accurately. Preliminary LeBail fitting carried out on the SPD data shows BBN is a tetragonal phase with a = 12.533(6) Å, c = 3.923(2) Å. On the basis of the systematic absences space group *P4bm* (No. 100) and *P4/mbm* (No. 127) were assigned. However, the non-centrosymmetric space group *P4bm* was excluded since the second harmonic generation (SHG) signal was not detected in the BBN sample. The starting *P4/mbm* model reported previously in paraelectric phase of $Pb_2K_{0.5}Li_{0.5}Nb_5O_{15}$[3] was used for refinements of SPD pattern, and barium, niobium and oxygen contents were fixed to the nominal stoichiometry. Crystallographic data of BBN refined from SPD pattern are listed in Table 1. The experimental, calculated, and difference profiles are shown in Fig. 1, and the refined structural parameters and crystal structure are shown in Table 2 and Fig. 2. The possible distributions of Ba^{2+} and Bi^{3+} in different A sites were tested in the refinement process. The big Ba atoms are prior to occupy A2 sites due to the negative convergence in A1 sites. Then the smaller Bi atoms reside in the rest of A sites. Compared to the Ba atom, smaller Bi seems to have irregular distribution in A1 and A2sites. The A1 sites are only occupied by 52.09% Bi, while the A2 sites are occupied by 24.95% Bi and 50.0% Ba, implying that about 1/3 of A sites are vacant, which is uncommon in TTB structure. The refinements for the room temperature (RT) data showed that the isotropic displacement factor U_{iso} for Bi atoms at A2 sites was abnormally large and the refinement of atomic anisotropic displacement factors (ADPs) for the Bi atoms at A2 sites improved the fitting remarkably. The prolate shapes of the thermal ellipsoids in Fig. 2(a), which are extremely large, suggest the split of Bi at the A2 sites. Finally, a

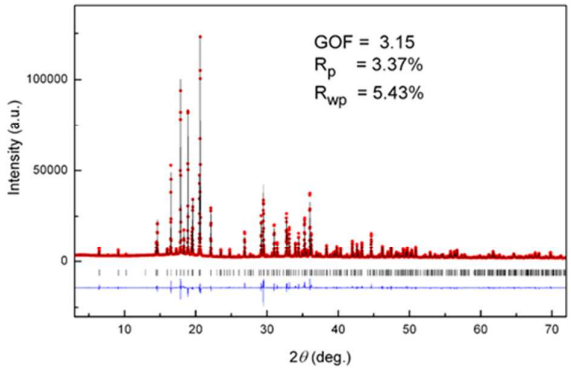

Fig. 1 Rietveld fit pattern for high-resolution synchrotron X-ray powder diffraction (SPD) data of BBN collected at RT with space group *P4/mbm*.

Table 1. Crystallographic Data of BBN Refined from SPD at room temperature.

	RT(SPD)
Rp	3.37%
Rwp	5.43%
χ^2	3.15
space group	*P4/mbm*
a (Å)	12.5337 (1)
c (Å)	3.9232(1)
15-coordinated site (A2)	24.95% Bi, 50.0% Ba, 25.05% vacancy
12-coordinated site (A1)	52.09% Bi, 48.91% vacancy

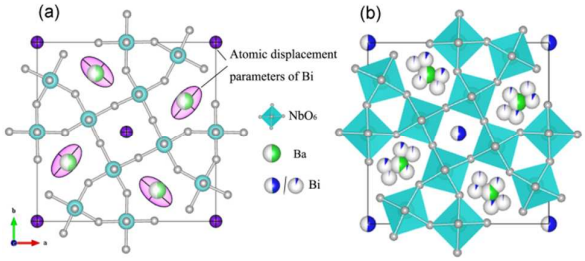

Fig. 2 (a) Schematic structure of BBN at RT refined with anisotropic displacement parameters. The large size of the ellipsoids in A2 site indicates the split of Bi atoms. (b) The final structure of BBN at RT with multiple-split of Bi in A2 sites.

Table 2. The Final Refined Structural Parameters of BBN at RT with Split of Bi in A2 sites

atom	Site	x	y	z	U_{iso} (Å^2)	Occupancy
Ba2	4h	0.6736(3)	0.1736(3)	0.5	0.0152 (7)	0.5
Bi2	8j	0.6169(17)	0.2457(27)	0.5	0.0077(97)	0.0251(3)
Bi2a	8j	0.5936(10)	0.1816(11)	0.5	0.0301(39)	0.0747(3)
Bi2b	4h	0.7867(18)	0.7133(17)	0.5	0.0290(8)	0.0499(3)
Bi1	2b	0	0	0.5	0.0847(13)	0.5209(3)
Nb1	2d	0	0.5	0	0.0109(6)	1
Nb2	8i	0.2114(1)	0.0740(1)	0	0.0116 (4)	1
O1	2c	0	0.5	0.5	0.0304(16)	1
O2	4g	0.2146(5)	0.7146(5)	0	0.0154(12)	1
O3	8i	0.0685(6)	0.1425(5)	0	0.0154(12)	1
O4	8i	0.0058(5)	0.3428(6)	0	0.0154(12)	1
O5	8j	0.7867(18)	0.7133(18)	0.5	0.0304(16)	1

multiple-split of Bi atoms in A2 sites was evolved, which was depicted as butterfly-like atomic clusters in Fig. 2(b). This split may be in correlation with the asymmetric electronic-shell environments of Bi cations with $6s^2$ lone pair. In the literature,[24,25] the substitution Bi^{3+}(1.16 Å, CN=8) in BBN by La^{3+}(1.17 Å, CN=8) (i.e. $BaLaNb_5O_{15}$) leads to lanthanum niobate impurities, indicating the split of Bi atoms in pentagonal cavities is in favor of the stability of tetragonal tungsten bronze particularly with large amount of cationic vacancies. The final refined chemical formula is $Ba_2Bi_{2.04}Nb_{10}O_{30}$, and the EDS gives the cations ratio of $Ba_2Bi_{1.89}Nb_{9.24}$ (error < 5%, shown in Table S1 in ESI†), suggesting the sample is stoichiometric. And The EDS mapping displays uniform elements distributions (Fig.S2). The phase also shows structurally stable at 800 °C in reducing conditions (Fig.S3, S4).

3.2 Electrical conductivity Characterization

Electrical conductivities of BBN, SBN and BBNT ceramics were measured by impedance spectroscopy using pellets fired at 1240 °C for 2 h. AC impedance spectroscopy normally resolves the grain (bulk), grain boundary, and electrode response according to their characteristic relaxation time showing successive semicircles in complex plane. Impedance data in the form of a complex plane plot for BBN, SBN and BBNT measured at 600 °C in air are shown in Fig. 3. BBN sample exhibited a single semicircle arc and a spike within

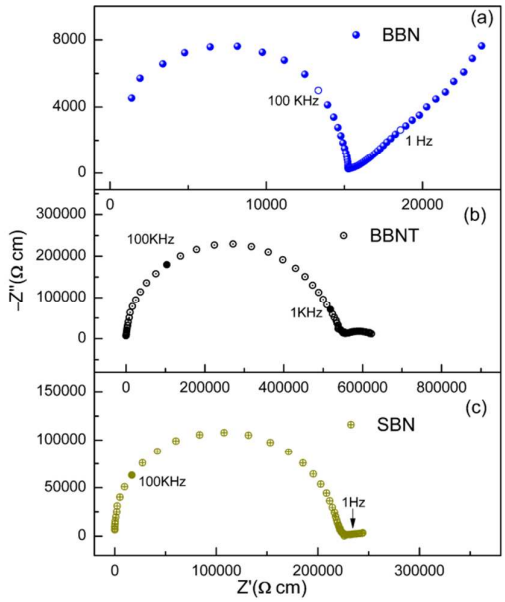

Fig. 3 Complex impedance plots for the BBN measured in air at 600 °C (a), and SBN at 600°C. (b) and BBNT at 600 °C (c). The low frequency tail or spike is ascribed to electrode response.

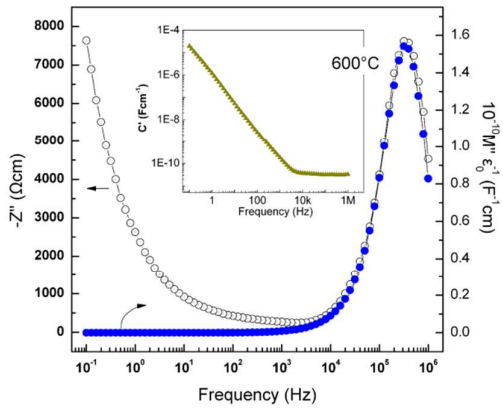

Fig. 4 Z''/M'' spectroscopic plots, and inset of the figure is C' spectroscopic plot at 600°C for BBN sintered for 2 hours.

the measured frequency range. The extracted ε_r is ~350, obtained from the single arc using the relation $\omega RC = 1$ at the arc maximum and the formula $C = \varepsilon_r\varepsilon_0 A/d$ (where ω is angular frequency corresponding to the maximum Z'', and A is the electrode area, d is sample thickness, ε_0 is the permittivity of free space). This is consist with the permittivity value of ~360 obtained from the temperature dependence of relative permittivity at fixed frequency (1MHz) as depicted in Fig. 7, indicating that the arc is associated with a bulk response.[26,27] The spike corresponding to Warburg electrode response was observed in the low frequency range 1-0.1 Hz, which shows a capacitance ~10^{-6}-10^{-5} F/cm and is assigned as ionic conduction response.[28] The spikes for SBN and BBNT, however, are not distinct, with relative larger resistivity 225 kΩcm^{-1}and 550 kΩcm^{-1}, respectively (the resistivity was estimated from the intercept of the semicircle arc at low frequency). We may speculate

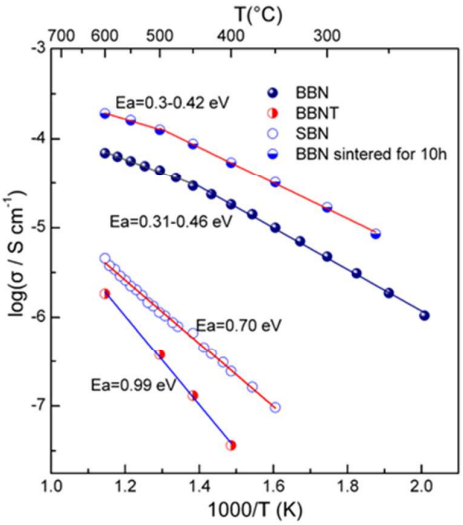

Fig. 5 Comparison of total electrical conductivity of the three TTB-structure BBN, SBN, BBNT pellets measured in air, which were sintered at 1240 °C for 2 hours, Conductivity data of BBN sintered at 1240 °C for 10 hours were also plotted for comparison

the electrical conductivity in BBN is dominated by ionic conduction compared with SBN and BBNT.

It is notable that no significant grain boundary contribution was observed in the impedance data for BBN at 600 °C, similar to lower temperatures (see Fig. S7). The impedance data were replotted as the imaginary parts of complex impedance Z'' and electric modulus, M'', against frequency on a double-logarithmic scale, Fig. 4. The maxima of M'' spectra are dominated by components with smallest capacitance, while the maxima in Z'' spectra are sensitive to components with largest resistance. The Z''/M'' curves show only a single Debye-type peak in both case with maxima at similar frequencies, indicating that the sample may be electrically homogeneous and could be represented by a single parallel RC element.[28] In addition, the overlap of the Z'' and M'' peak in the spectra reflects the domination of long-range migration of ions at 600 °C.[29] Capacitance, C', as a function of frequency (See Fig.4 inset section) showed a frequency-independent plateau at high frequency region which corresponds to the bulk response with relative permittivity values ~360.

The Arrhenius plots of TTB-type BBN, SBN, and BBNT are shown in Fig. 5. Conductivity data of BBN sintered at 1240 °C for 10 h were also plotted for comparison. The total conductivity of BBN sintered at 1240 °C for 10 h varies within 10^{-5}- 3×10^{-4} S/cm, with an activation energy of 0.3-0.42 eV over the 250 – 600 °C range. SBN and BBNT ceramics show lower conductivities and larger activation energies. The relative low activation energy for BBN is unusual in TTB compounds, which will be discussed in Section 3.4 below.

The impedance spectroscopy measurement was employed under different gas atmospheres (see Fig. S5). There's no distinct change in bulk electrical conductivity at 550 °C by varying the p_{O2} from Air to Ar gas. When measured in 10%H_2/90%N_2, however, the ceramic showed a much lower resistance indicative of some n-type electronic conductivity at more reducing atmospheres. It could be concluded that the migration ions are oxygen ions. The ionic transport number was evaluated to be 0.66 - 0.94 at 250 - 600 °C in

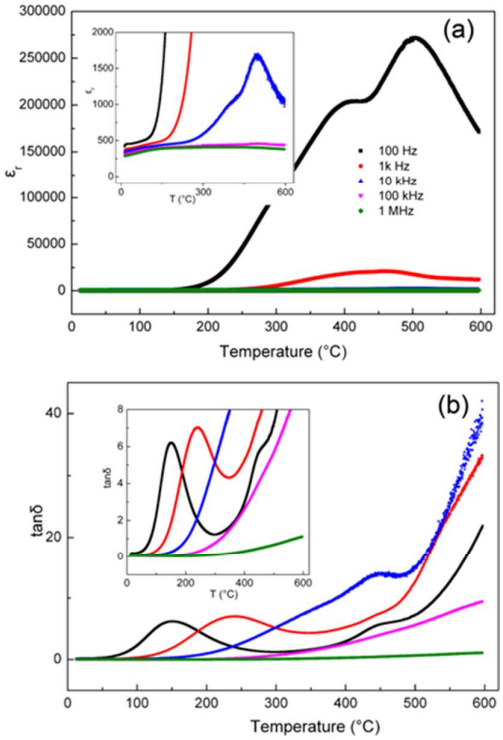

Fig. 6 The temperature dependences of the dielectric permittivity ε_r (a), and loss tan δ (b) at different fixed frequencies from 100 Hz to 1 MHz for BBN pellets sintered for 2 hours at 1240 °C. Insets are an expanded view of data between RT and 600 °C.

air (see Fig. S8). Actually, the SBN ceramic would show larger ionic conductivity due to smaller Sr^{2+} ions if the migration ions are Ba^{2+} ions in BBN ceramic.

3.3 Dielectric Properties

The temperature dependence of the permittivity ε_r and dielectric loss tan δ for BBN at fixed frequencies of 0.1, 1, 10, 100 kHz and 1 MHz over the temperature range from RT to 600°C are shown in Fig. 6. Two giant permittivity peaks of ~2×10^5 and 2.8×10^5 at 100 Hz at 400 °C and 600 °C respectively can be observed, while at higher frequencies(>10kHz), no peaks are observed. This phenomenon is in accordance with capacitance data as a function of frequency in Fig. 4 (inset section), which shows a sharp increase as the frequency decreases. The giant permittivity peaks are not the associated with the intrinsic bulk response but the Warburg electrode response that arise from the formation of electric double layers at the electrode-sample interface. This also confirms the ionic conduction in BBN. Loss tan δ peaks at low frequencies (<10 kHz) below 500 °C are observed. The dielectric relaxation peaks may be associated with the short-range hopping of oxygen vacancies, since oxygen vacancies are active at low frequency and act as " polarons", similar to the reorientation of the dipole. [30,31]

The temperature dependences of the dielectric permittivity ε_r, and loss tan δ at 1 MHz for BBN, SBN, BBNT and BBN10 (sintered at 1240 °C for 10 h pellets between RT to 600 °C are shown in Fig. 7. There are no sharp dielectric peaks in these TTB compounds, Fig. 7 (a), due to their paraelectric properties above room temperature

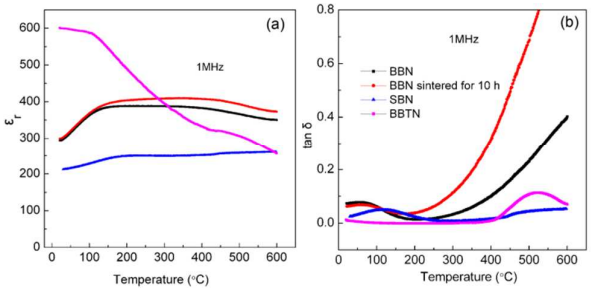

Fig. 7 Temperature dependence of ,(a) dielectric permittivity ε_r and, (b) loss tan δ at 1MHz from RT to 600 °C for BBN, BBN10h, SBN, and BBNT. The BBN10h pellet was sintered at 1240 °C for 10 hours, and others for 2 hours with a impedance analyzer Agilent 4294A.

since these compounds exhibit typical relaxor behaviors with broad phase transition T_m, which is lower than the room temperature.[32] It can be seen that the dielectric loss of BBN is much larger than SBN and BBNT, indicative of the higher conductivity associated with ion conduction in BBN. In contrast, the dielectric loss markedly increased for BBN with the extension of sintering time from 2 h to 10 h. The large dielectric loss may arise from the oxygen vacancies generated from volatilization loss of Bi_2O_3 during the ceramic processing in terms of the Kroger-Vink equation,[26, 27]

$$2Bi_{Bi}^{\times} + 3O_O^{\times} \rightarrow 2V_{Bi}^{'''} + 3V_O^{\cdot\cdot} + 2Bi_2O_3$$

The increase in dielectric loss and total electrical conductivity with the extension of sintering time may derive from the more loss of Bi_2O_3. Unfortunately, the loss amount is too small to be measured using the common chemical techniques such as ICP and EDS.[26] Other migration ion species can be excluded since the bulk conductivity would not increase significantly with the extension of sintering time.

3.4 Conduction Mechanism

Why BBN ceramic shows larger oxide ion conductivity compared with SBN and BBNT is an intriguing issue. It can be noted that the larger cell parameters of BBN compared with SBN (see Fig. S6in ESI†) can provide more free space for oxide ions hopping since ionic radius of Ba (1.61 Å, CN=12) is much larger than that of Sr (1.44 Å, CN=12).[33] This may be associated with the relative low enthalpies for oxide ion hopping or activation energy as mentioned above. The smaller, stiffer lattices of SBN give less dynamics and oxide ions mobility decreases. This is analogous to the situation that Gd-doped CeO_2 shows much larger oxide ion conductivity compared with Y-doped ZrO_2.[11]

On the other hand, the cationic vacancy accounting for about 1/3 of total A sites for BBN, which is different from perovskite structured compounds with fully-occupied A sites, may also increase the oxide ion mobility. When the A sites of a TTB type compound are fully filled with cations, for example, in BBNT, the conductivities decrease significantly and activation energy increases obviously (see Fig. 5 and Fig. S7 in ESI†). Such cationic vacancies in BBN may be responsible for the lower activation energy ~0.3 - 0.5eV.Actually many Bi-based oxide compounds[26,34-37] are oxide ion conductors. The highly polarizable cation Bi^{3+} whose $6s^2$ lone pair electrons are known to be highly stereochemically active and hybridized easily, is suitable for anion migration, and the formation of oxygen defects is favored by the weak Bi-O bond. For BBN, the multiple-split of Bi atoms in A2 sites brings about a variety of Bi-O bond lengths (See Table S2 in ESI†). This may facilitate the oxide ions migration.

4. Conclusions

The work reveals that a Bi-based TTB-type oxide, $BaBiNb_5O_{15}$, exhibits an oxygen ion conductivity of 3×10^{-4} S/cm at 600 °C with relative low E_a (0.3-0.5eV), which shows the best oxide ion conductivity among TTBs. The structure was determined by high-resolution synchrotron X-ray powder radiation and the compound crystallizes in the tetragonal centric space group *P4/mbm* with *a* = 12.5337(1) Å and *c* = 3.9232(1) Å. Electrical properties were studied by impedance spectroscopy and the dielectric properties were also discussed. It is suggested that the large amount of cationic vacancies in A sites, the big free space created by the large Ba^{2+}cations, and the split of Bi atoms (significant polarisability) may be in favor of oxygen ion migration. This study shows that TTB oxides may be a new-type of oxygen ion conductivity materials.

Acknowledgements

This work was supported by the National Natural Science Foundation of China (grant no. 91022016, 91422301, and 21231001), the Program for Changjiang Scholars and the Innovative Research Team in University (IRT1207), and the Fundamental Research Funds for the Central Universities, China (Grant No. FRF-SD-13-008A). We thank Liuzhen Bian from University of Science and Technology Beijing for their help in the complex impedance measurement at different atmospheres.

References

1 P. B. Jamieson, S. C. Abrahams, J. L. Bernstein, *J. Chem. Phys.*, 1968, **48**, 5048−5056.
2 K. Lin, H. Wu, F. Wang, Y. Rong, J. Chen, J. Deng, R. Yu, L. Fang, Q. Huang, X. Xing, *Dalton Trans.*, 2014, **43**, 7037−7043.
3 K. Lin, Y. Rong, H. Wu, Q. Huang, L. You, Y. Ren, L. Fan, J. Chen, X. Xing, *Inorg. Chem.*, 2014, **53**, 9174–9180.
4 P. B. Jamieson, S. C. Abrahams, J. L. Bernstein, *J. Chem. Phys.*, 1969, **50**, 4352−4363.
5 J. Gardner, F. D. Morrison, *Dalton Trans.*, 2014, **43**, 11687-11695.
6 C. A. Kirk, M. C. Stennett, I. M. Reaney, A. R.West, *J. Mater. Chem.*, 2002, **12**, 2609−2611.
7 R. R. Neurgaonkar, J. R. Oliver, W. K. Cory, L. E. Cross, D. Viehland, *Ferroelectrics*, 1994, **160**, 265-276.
8 R. J. Xie, Y. Akimune, *J. Mater. Chem.*, 2002, **12**, 3156−3161.
9 J. H. Ko, S. Kojima, S. G. Lushnikov, R. S. Katiyar, J. H Kim, J. H. Ro, *J. Appl. Phys.*, 2002, **92**, 1536−1543.
10 P. Ganguly, S. Devi, A. K. Jha, K. L. Deori, *Ferroelectrics*, 2009, **381**, 111−119.
11 L. Malavasi, C. A. J. Fisher, M. S. Islam, *Chem. Soc. Rev.*, 2010, **39**, 4370−4387.

12 P. Vernoux, L. Lizarraga, M. N. Tsampas, F. M. Sapountzi, A. De Lucas-Consuegra, J. L. Valverde, S. Souentie, C. G. Vayenas, D. Tsiplakides, S. Balomenou, E. A. Baranova, *Chem. Rev.*, 2013, **113**, 8192−8260.

13 J. Sunarso, S. Baumann, J. M. Serra, W. A. Meulenberg, S. Liu, Y. S. Lin, J. C. Diniz da Costa, *J. Membr. Sci.*, 2008, **320**, 13−41.

14 B. C. H. Steele, A. Heinzel, Nature, 2001, **414**, 345–352.

15 T. Ishihara, H. Matsuda, Y. Takita, *J. Am. Chem. Soc.*, 1994, **116**, 3801−3803.

16 D. J. L. Brett, A. Atkinson, N. P. Brandon, S. Skinner, *Chem. Soc. Rev.*, 2008, **37**, 1568–1578.

17 M. S. Khan, M. S. Islam , D. R. Bates, *J. Phys. Chem. B*, 1998, **102**, 3099–3104.

18 M. S.Islam, *J. Mater. Chem.*, 2000, **10**, 1027−1038.

19 J. A. Kilner, R. J.Brook, *Solid State Ionics*, 1982, **6**, 237−252.

20 R. L. Cook, A. F. Sammells, *Solid State Ionics*, 1991, **45**, 311−321.

21 Kaiser, J. L. Bradley, P. R. Slater, J. T. S. Irvine, *Solid State Ionics*, 2000, **135**, 519–524.

22 M. Prades, N. Masó, H. Beltrán, E. Cordoncillo, A. R.West, *Inorg. Chem*., 2013, **52**, 1729−1736.

23 X. Kuang, F. Pan, J. Cao, C. Liang, M. R. Suchomel, F. Porcher, M. Allix, *Inorg. Chem.*, 2013, **52**, 13244−13252.

24 K. Masuno, *J. Phys. Soc. Jpn*., 1964, **19**, 323-328.

25 J. K. Wang, N. Wakiya, K.Shinozaki, N. Mizutani, *Electroceramics in Japan III*, 2000, **181–182**, 31−34.

26 M. Li, M. J. Pietrowski, R. A. De Souza, H. Zhang, I. M. Reaney, S. N. Cook, J. A. Kilner, D. C. Sinclair, *Nat. Mater.*, 2014, **13**, 31−35.

27 M. Li, H. Zhang, S. N. Cook, L. Li, J. A. Kilner, Ian. M. Reaney, D. C. Sinclair, *Chem. Mater*., 2015, **27**, 629–634.

28 J. T. S. Irvine, D. C. Sinclair, A. R. West, *Adv. Mater*., 1990, **2**, 132−138.

29 R. Gerhardt, *J. Phys. Chem. Solids*., 1994, **55**, 1491−1506.

30 C. Ang, Z. Yu and L. E. Cross, *Phys. Rev. B: Condens. Matter Mater. Phys.*, 2000, **62**, 228−236.

31 X. P. Wang, Q. F. Fang, Z. S. Li, G. G. Zhang and Z. G. Yi, *Appl. Phys. Lett*., 2002, **81**, 3434–3436.

32 A. Simon, J. Ravez,. *physica status solidi (a)*, 2003, **199**, 541–545.

33 R. D. Shannon, *ActaCrystallogr., Sect. A: Cryst. Phys., Diffr., Theor. Gen. Crystallogr*., 1976, **32**, 751–767.

34 J. C. Boivin, G. Mairesse, *Chem. Mater*, 1998, **10**, 2870–2888.

35 X. Kuang, J. L. Payne, J. D. Farrell, M. R. Johnson, I. R. Evans, *Chem. Mater*., 2012, **24**, 2162–2167.

36 Y. Li, T. P. Hutchinson, X. Kuang, P. R. Slater, M. R. Johnson, I. R. Evans, *Chem. Mater*., 2009, **21**, 4661–4668.

37 S. Sanna, V. Esposito, J. W. Andreasen, J. Hjelm, W. Zhang, T. Kasama, S. B. Simonsen, M. Christensen, S Linderoth, N. Pryds, *Nat. Mater*., 2015, **14**, 500–504.